remote sensing

MDPI

Article

Estimation of Forest Fire Burned Area by Distinguishing Non-Photosynthetic and Photosynthetic Vegetation Using Triangular Space Method

Xiaoqiong Wang [1,2,†], Jun Yan [3,†], Qingjiu Tian [1,2], Xianyi Li [3], Jia Tian [1,4,*], Cuicui Zhu [1,2] and Qianjing Li [1,2]

[1] International Institute for Earth System Science, Nanjing University, Nanjing 210023, China; mg21270088@smail.nju.edu.cn (X.W.); tianqj@nju.edu.cn (Q.T.); mg21270097@smail.nju.edu.cn (C.Z.); liqj@smail.nju.edu.cn (Q.L.)
[2] Jiangsu Provincial Key Laboratory of Geographic Information Science and Technology, Nanjing University, Nanjing 210023, China
[3] Zhuhai Orbita Aerospace Science & Technology Co., Ltd., Zhuhai 519080, China; yan@myorbita.net (J.Y.); lixianyi@myorbita.net (X.L.)
[4] School of Instrumentation and Optoelectronic Engineering, Beihang University, Beijing 100191, China
* Correspondence: tianjia@buaa.edu.cn
† These co-authors contributed equally to this work.

Abstract: The forest fire burned area is one of the most basic factors used to describe forest fires and plays a vital role in damage assessment. The development of the NSSI-NDVI vegetation index triangular space method enables simultaneous calculation of the flammable non-photosynthetic vegetation (NPV), combustible photosynthetic vegetation (PV), and incombustible bare soil (BS) fractional cover in forest areas. This can be used to compensate for the calculation method that was based on NDVI vegetation index only by comparing vegetation cover before and after forest fires, with the omission of the NPV burned area. To this end, the NSSI-NDVI triangular space shape consistency before and after forest fires was elucidated through combustion and ash wetting experiments. In addition, the feasibility of the NSSI-NDVI triangular space method for the accurate calculation of the post-fire vegetation damage area was verified. Finally, the applicability and accuracy of this research method were verified based on 10 m spatial resolution satellite hyperspectral images from before and after the forest fire in Lushan, Sichuan Province, China. The NSSI-NDVI triangular space method was used to calculate the PV, NPV, and BS coverage simultaneously, and component transformation was used to calculate the burned area and burned site separately.

Keywords: forest fire; hyperspectral remote sensing; burned area; non-photosynthetic vegetation; triangular space method

Citation: Wang, X.; Yan, J.; Tian, Q.; Li, X.; Tian, J.; Zhu, C.; Li, Q. Estimation of Forest Fire Burned Area by Distinguishing Non-Photosynthetic and Photosynthetic Vegetation Using Triangular Space Method. *Remote Sens.* **2023**, *15*, 3115. https://doi.org/10.3390/rs15123115

Academic Editor: Ioannis Z. Gitas

Received: 11 April 2023
Revised: 31 May 2023
Accepted: 12 June 2023
Published: 14 June 2023

1. Introduction

In many ecosystems, fire is a natural disturbance that helps promote diversity and natural regeneration [1]. At regional and local scales, fire has significant socio-economic impacts on life and property [2]. For example, fire affects carbon budgets [3,4] and vegetation succession [5], which is also an important driver of land use transformation [6]. As one of the most dominant vegetation types on land, forest plays an important role in the nature [7]. Unfortunately, forest fires, which occur with great frequency [8] and quite destructively, are among the threats to valuable forest resources. Forest fires have become a serious natural danger [9]; therefore, the prevention and control of forest fires and post-fire assessment are important.

Remote sensing has been extensively used by many researchers to study fire occurrence at global, regional, and local scales [10]. Compared to post-fire field measurements, remote-sensing-based measurement is a more affordable option [11]. It is able to overcome

the limitations of inconsistent and incomplete temporal–spatial data for wildfire information [12], and is especially suitable for monitoring large and topographically complex landscapes [11]. Currently, estimating the burned area using remote sensing data is mainly based on spectral indices [13–15] and radiative transfer models (RTM) [16–18]. Chiang et al. used S3-SLSTR and VIIRS-DNB images to estimate the burned area by spectral indices including normalized difference vegetation index (NDVI), normalized difference moisture index (NDWI), and normalized burn ratio (NBR) [19]; dos Santos et al. used the differential normalized burn ratio (dNBR) and relative differential normalized burn ratio (RdNBR) to assess fire severity and regeneration [20]. In addition, spectral mixture analysis (SMA), multiple endmember spectral mixture analysis (MESMA), and linear spectral mixture analysis (LSMA) have been greatly applied and developed, and the burned area calculation using these methods has good performance with multiple precision and multi-field data [21,22].

With the application and development of remote sensing technology, in order to assess land cover and vegetation type changes due to fire [23], more detailed burned area estimation and mapping has become one of the needs [24]. Forest ecosystems include photosynthetic vegetation (PV), non-photosynthetic vegetation (NPV), and bare soil (BS), as well as water bodies, shade, and some other types of land cover. PV, NPV, and BS have different spectral features and combustion characteristics [25]. NPV, including forest fine fuel, is an important parameter in determining forest fire ignition, combustion, and behavior [26], and it also plays a key role in terms of fire risk and frequency, wind, and water erosion [27,28]. NPV has been less frequently incorporated in previous studies about burned area estimation. In contrast, traditional spectral index methods are based mainly on the vegetation–soil dimidiate pixel model [29], and focus on pre-fire versus post-fire changes in vegetation. These methods ignore changes in PV and NPV due to variations in fire severity, which may cause confusion between the original NPV and terrestrial objects whose traits have changed due to fire drying and therefore exhibit characteristics of NPV. Thus, the assessment of vegetation loss due to forest fire damage is typically overestimated [30]. After compensating for the effects of water bodies and shadows, and based on the idea of mixed PV, NPV, and BS image pixels, Cochrane et al. proposed a method for detecting and classifying burned forests using the maximum differentiability of the NPV fraction to distinguish different types of forests [31]. The results show that NPV is suitable for analyzing forest fires and confirm that NPV can be applied for accurate fire assessment. Forest fires also cause irregular changes from green vegetation to NPV [32–34] and BS, indicating the direction and range of fire movement. Combining PV and NPV for forest fire damage assessment is vital for forest fire prevention and to construct of fire prediction and early warning systems [35], as well as to help guide the development of ecosystem restoration projects.

In this paper, we acquired spectral reflectance of NPV, PV, and burned ash through combustion experiments, and analyzed the scatter distribution of varied targets in the NSSI-NDVI triangular space. The NSSI-NDVI triangular space variability of the mixed pixels pre- and post-fire was elucidated, and the feasibility of the NSSI-NDVI triangular space method for accurate calculation of post-fire vegetation damage area was verified. In addition, based on the Zhuhai-1 satellite hyperspectral data (OHS) with 10 m spatial resolution, a component transformation was constructed pre- and post-fire. Whether the fire process contains PV converted to NPV, the area is divided into the burned area (containing PV converted to NPV, and BS, NPV converted to BS) and burned site (only the increased part of BS). Both burned area and burned site are vital for systematic monitoring and comprehensive control of forest fires. However, they have varying levels of significance for assessing fire size and actual damage. The forest fire burned area is the affected area where the fire was extinguished after the surface fire [36,37]. It is the most basic descriptor of forest fires [38], and accurately estimating and mapping of its area is essential for quantifying carbon budgets [39–41]. On the other hand, the forest burn site is the post-fire damaged area that has burned down completely [42]. It contributes to assessing the impacts and losses of fire [23,43].

In addition, the NSSI-NDVI triangular space method was used to perform image pixel unmixing to calculate the pre- and post-fire PV, NPV, and BS coverage of the study area simultaneously. This enables an accurate estimation of forest fire burned area and burned site by distinguishing PV from NPV. Finally, the applicability and accuracy of the study method was verified.

2. Methodology

2.1. NPV-BS Separation Index Selection

We use the triangular space method [44] to distinguish NPV from PV. Compared with the traditional vegetation index reflectance estimation [45], measuring the relative coverage of PV, NPV, and BS can be more useful to estimate the loss caused by fire [46], which may lead to a better assessment of forest fire severity and damage.

Relying on two near-infrared bands, Jia Tian et al. [47] constructed the NPV-Soil Separation Index (NSSI) for NPV and BS separation. The NSSI was devised to capture the spectral difference between NPV and BS around 820 nm. Considering the design of the Zhuhai-1 OHS sensor and optimizing the band selection, the reflectance (R) of band 27 (centered at 865 nm) and band 22 (centered at 776 nm) of Zhuhai-1 OHS satellite group 03 are used to calculate the NSSI:

$$NSSI_{OHS} = \frac{R_{865} - R_{776}}{R_{865} + R_{776}} \tag{1}$$

Using the pixel unmixing algorithm, the PV, NPV, and BS coverage of each pixel is calculated based on the following algorithm [48]:

$$\begin{gathered} f_{NPV} + f_{PV} + f_{BS} = 1 \\ NDVI_M = f_{NPV} \times NDVI_{NPV} + f_{BS} \times NDVI_{BS} + f_{PV} \times NDVI_{PV} \\ NSSI_M = f_{NPV} \times NSSI_{NPV} + f_{BS} \times NSSI_{BS} + f_{PV} \times NSSI_{PV} \end{gathered} \tag{2}$$

where f_{NPV}, f_{PV}, and f_{BS} are the coverage of the three endmembers to be solved; $NDVI_{NPV}$, $NDVI_{BS}$, $NDVI_{PV}$, and $NDVI_M$ are the NDVI values for the three endmembers and the hybrid pixel, respectively; and $NSSI_{NPV}$, $NSSI_{BS}$, $NSSI_{PV}$, and $NSSI_M$ are the NSSI values of the three endmembers and the hybrid pixel, respectively.

2.2. Experimental Design and Spectral Measurements

2.2.1. Experimental Design

In this paper, a total of three experiments were conducted. Two of them are PV and NPV simulated combustion experiments, and the third is the ash of NPV and PV wetting experiment.

Simulated combustion experiments are designed to investigate the changes of PV reflectance spectra caused by the fire process how to change NSSI-NDVI triangular space, and the influence of the post-forest fire traces on the calculation of three-component abundance. Different types of PV and NPV were selected for the fire simulation experiments as samples to simulate the process of the forest gradually igniting from the ignition point and spreading to eventually form burned area. Finally, we obtained and classified PV, NPV fire samples with different burning levels, ash with different grain sizes, etc.

In addition, the ash of NPV and PV wetting process was simulated by combining the characteristics that make the ash easily get wetted after the occurrence of forest fires. According to the difference in particle size of the ash produced by the fire simulation experiment, they were divided into three groups, and the surface was sprayed with water in mist five times (on the one hand, to simulate the actual rain in nature, and on the other hand, to make the surface water more uniform) (Figure 1). Then, wet fire samples with equal proportional increases in water content were obtained.

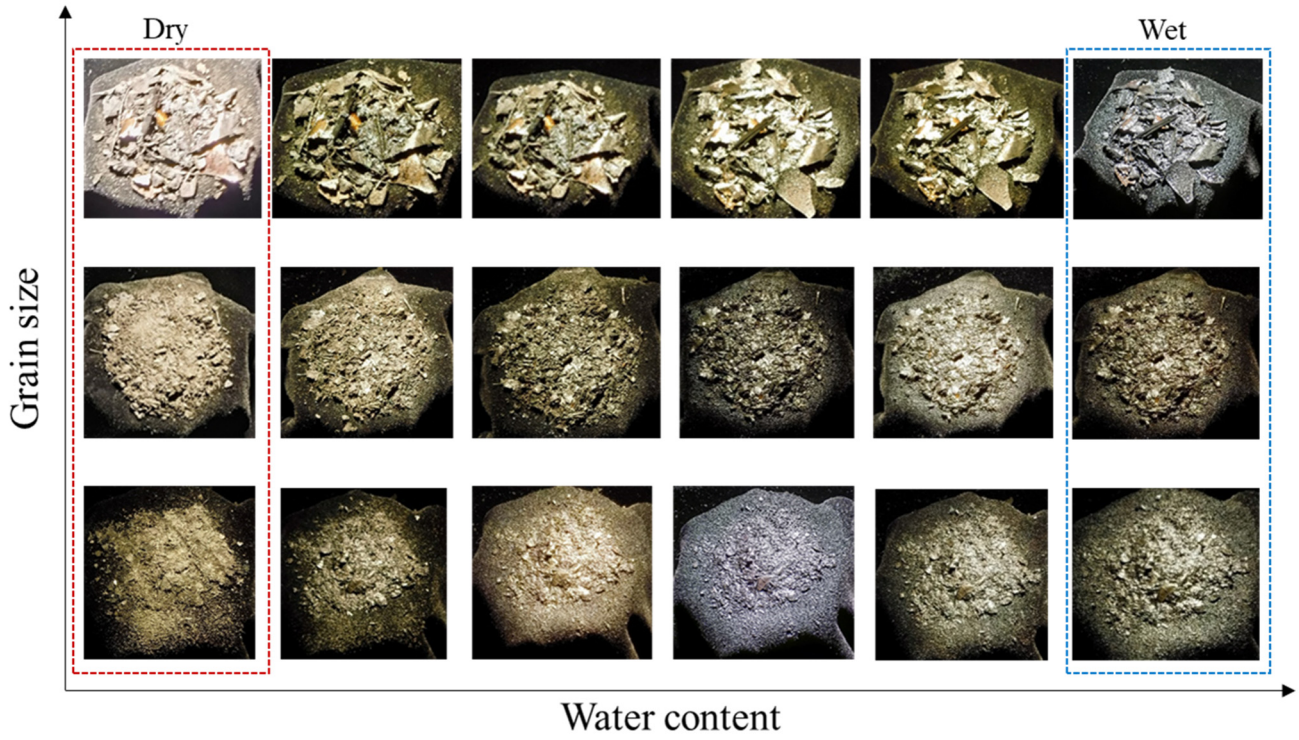

Figure 1. Schematic diagram of different particle size fire ash with wetting experiment.

2.2.2. Spectral Measurements

Spectral data of typical NPV, BS, and PV were obtained from the international common feature spectral library or laboratory spectral measurements. The spectral measurement samples of typical vegetation and NPV were obtained from field sampling or simulation experiments. The samples were measured in a dark room using an ASD Illuminator Reflectance Lamp for the experiment in the room unchanged. The ASD Fieldspec 4 spectroradiometer was equipped with a 5° field-of-view fore optic, and the optic was mounted 10 cm above the sample. Five measurements were made for each sample after the white reference panel calibration, and the average value was obtained. Finally, the measured spectra were processed with splice correction. The BS samples were selected from the ISRIC-ICRAF soil VNIR spectral library because of the insignificant changes in the spectral characteristics of BS before and after fire. Five spectra collected in China were selected, and these spectral curves were measured in the lab between 400 nm and 2500 nm at 10 nm intervals.

As shown in Figure 2, the fire ash with different particle sizes in the water addition experiment had obvious absorption peaks near 1900 nm. As the level of water addition increases, the reflectance of the fire ash after the water addition changes less. The water addition experiment shows that the amount of water addition has little effect on the spectral characteristics of the ash due to the small magnitude.

The spectral curves (Figure 3) during the combustion process showed that the darkened black leaves after the fire lost chlorophyll. The lamellar structure of the leaves was largely destroyed, and the NIR reflectance was low. The reflectance of the full spectrum of the fire ash were low, and the spectral curves of the overfired black leaves and the black burned area were different, and there were also differences in the spectra of the gray and black burned area.

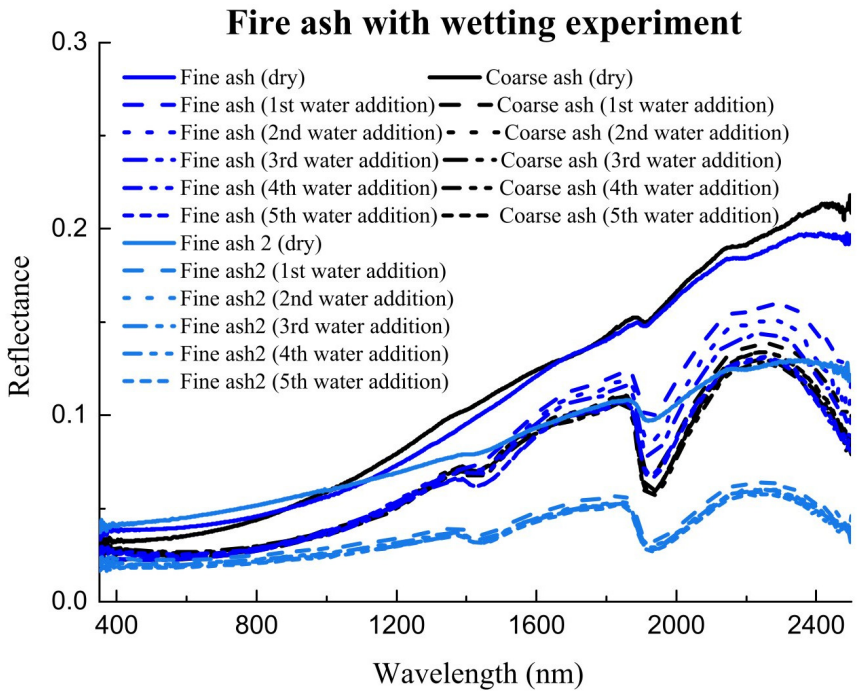

Figure 2. Spectral reflectance of different particle size fire ash with wetting experiment.

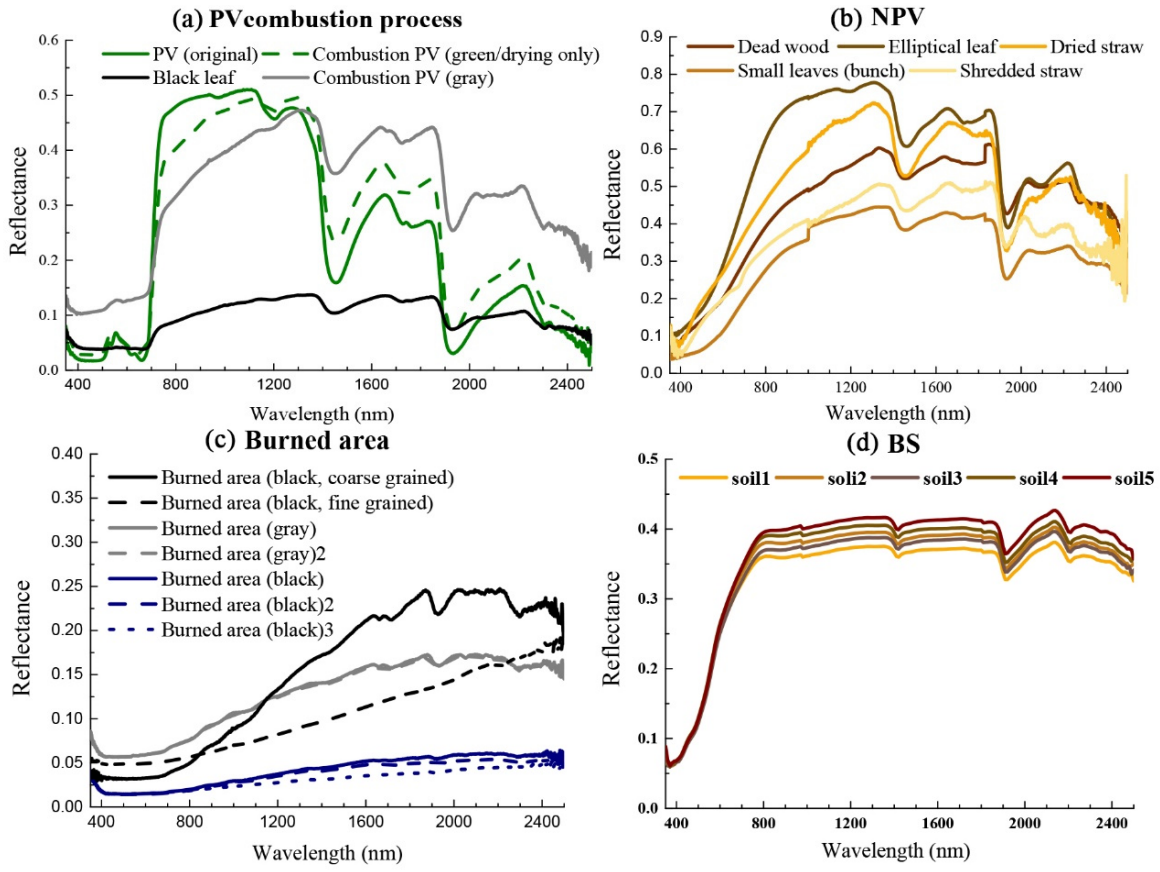

Figure 3. Spectral reflectance of: (**a**) Samples of PV combustion process, (**b**) Samples of NPV, (**c**) Samples of burned area with different particle sizes and colors, (**d**) Samples of soil.

3. Results

3.1. Laboratory Results

3.1.1. Pre- and Post-Fire NSSI-NDVI Triangular Space

Based on the spectral information collected by the ASD spectroradiometer, the spectral indices of each sample were calculated, and the NSSI-NDVI triangular space was established (Figure 4) to observe its distribution characteristics. It was found that post-fire, the PV and BS in the original background were not considered, and triangular features were also formed as far as the fire process was concerned. The NSSI-NDVI triangular space still existed (triangular space still existed), indicating the applicability of using the triangular space method to extract post-fire coverage.

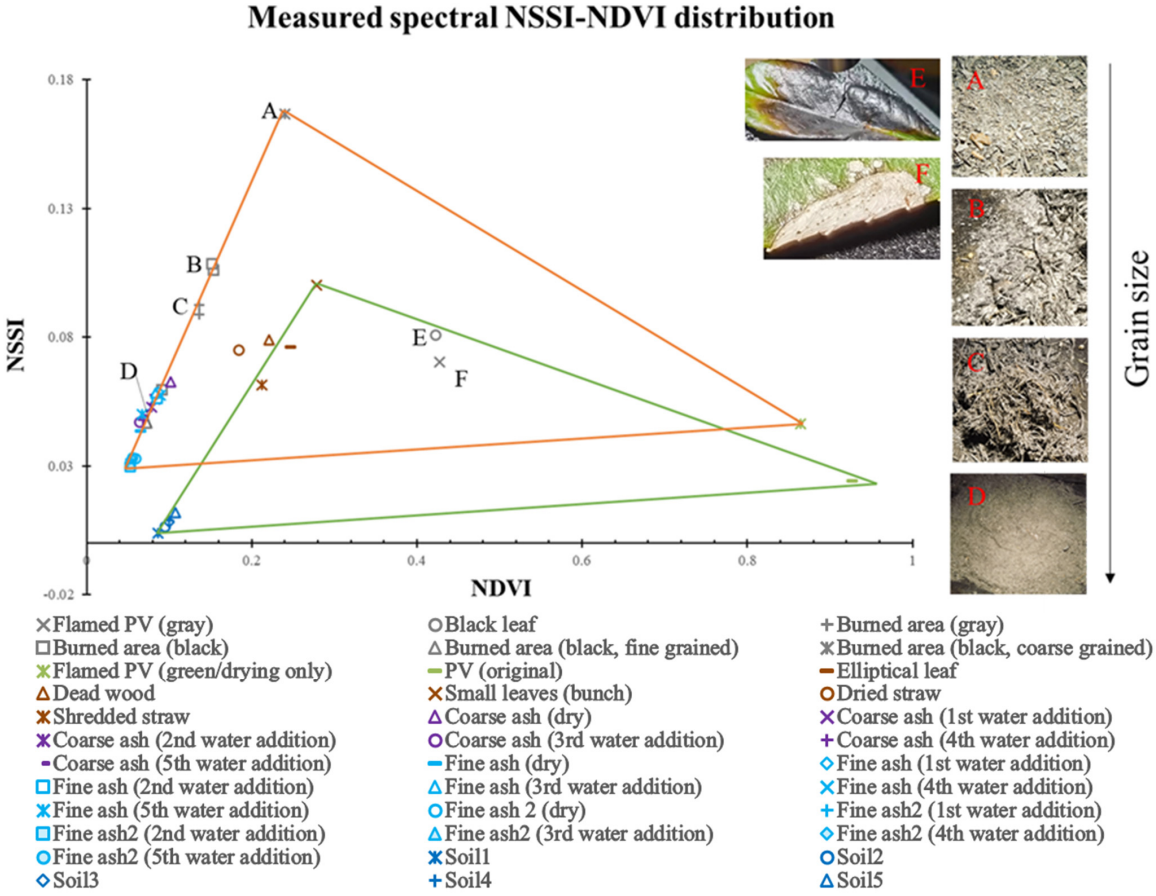

Figure 4. Spatial distribution of NSSI-NDVI features from experimental measurements and standard sample spectra: (A–F) are representative samples in the experiment (legend for names), and their appearance, such as color, and other morphology correlate with their distribution in the left triangle (Triangles) are NSSI-NDVI triangle features of samples (green for pre-fire, orange for post-fire).

In terms of endmember movement, the PV that still retained the characteristics of PV after drying after the experiment was still located at the right vertex of the triangle. While the fire ash with larger particle size interspersed with unburned PV moved to the location of the NPV endmember. As the particle size of the fire ash gradually became finer, and closer to the BS endmember location, the ash of different particle sizes moved from the NPV endmember to the BS endmember location along the line connecting the NPV and BS endmembers, from large to small. The triangle after the overall experiment showed a shift to the left and upward. The component conversion was from PV to BS, moving counterclockwise inside the triangle. In terms of index value changes, the NSSI values of the fire ash after water addition are all small and converge to the endmember as BS, while the NSSI values of the BS before burning are also small, with only a slight difference

in NDVI (NDVI values of the BS pre-fire are larger than NDVI values of the fire ash). From the distribution position, the pre-fire BS is at the lower left position of the triangular space, while the fire ash produced by the fire process, regardless of the wetness, are also gathered at the lower left position of the triangle. This reflects the greatest characteristic of the fire process: the increase in BS. This aggregation feature triggered consideration of the relationship between the movement of the components in the fire process and laid the foundation for using the algebraic relationship of the component coverage pre- and post-fire to find the changes. In addition, the experiment also found that the PV, NPV, and BS with different combustion degrees were distributed longitudinally in the NSSI direction, and the differences in their NSSI values could be used to extract areas with different combustion degrees (burned area and burned site separation).

3.1.2. Changes in the Abundance of Each Component Pre- and Post-Fire

Fuel characteristics can have different effects on fire head intensity and spread rate [49,50]. The water content of fine fuel (belonging to NPV) determines the ease of burning fuel [51–53]. Due to the different combustion characteristics, NPV with low water content is more flammable when exposed to fire, whereas healthy PV with high water content is less flammable. NPV is the first to burn in a fire and ignites PV. With long burning times, both PV and NPV are transformed into gray-black BS with no clear reflectance spectrum corresponding to terrestrial objects. Burning time is short and ignition may be incomplete (leading to baked PV), but the heat leads to the loss of the original pigments and yellowing, dehydration, and wilting. In the end, PV is transformed into NPV.

We combine the concepts of forest burn site and burn area and introduce NPV into our fire studies. In this paper, burned sites represent the area where the original fractional terrestrial object type is completely burnt by the fire, and burned area is defined as areas where both PV and NPV are converted to BS. Similarly, the burned area represents the area where the original fractional terrestrial object coverage is changed by burning in the fire. In addition to the area of the burned site, the burned area also includes areas where PV converted to NPV. The interconversion of terrestrial objects decreases each type of land coverage for different reasons, whereas an increase in land coverage originates from the conversion of different types of land coverage (Figure 5). This phenomenon is responsible for the difference in land coverage fractions due to the fire and the transformation between fractions.

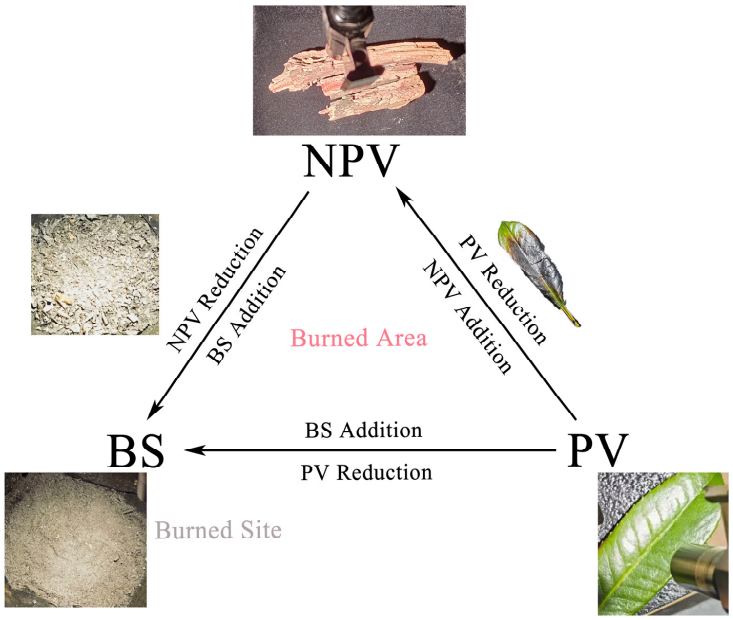

Figure 5. Schematic diagram of fraction conversion and corresponding typical samples.

3.2. Satellite Image Data Results

3.2.1. Study Area and Data Processing

The study area is the Lushan Mountain range and its surroundings in Xichang City (102°16′E–102°20′E, 27°47′N–27°52′N) of Liangshan County, Sichuan Province, China. The Lushan Mountain range (Figure 6) has an elevation of 2317 m, and the topography is generally high in the east and low in the west, high in the south and low in the north. Purple and anthropogenic soils are the most dominant soil types [54]. It has a subtropical highland monsoon climate with abundant precipitation from May to October, which makes the forest cover of Lushan reach extremely high elevations. The region is rich in subtropical dry evergreen broad-leaved forests and evergreen coniferous forests (*Cyclobalanopsis glaucoides Schotky*) and has developed a complete tree and grassland layer mainly with a scrub layer. Due to the large daily temperature difference, small annual temperature difference, less snow and ice, more sunshine, moderate heat and cold in Lushan, PV and NPV coverage do not undergo significant seasonal variations. NPV, PV, and BS are unevenly distributed throughout the state of Liangshan County, Sichuan Province, which corresponds to the topography of the area and the distribution of each category. Overall, BS coverage is greater at the central and eastern edges of Liangshan Prefecture, whereas NPV is widely distributed in the northeast and southwest. NPV and PV form a north–south spaced cross-distribution zone in the northwest. The fire occurred in the main part of the Lushan Mountain range, which is in the middle of the region in the north–south direction.

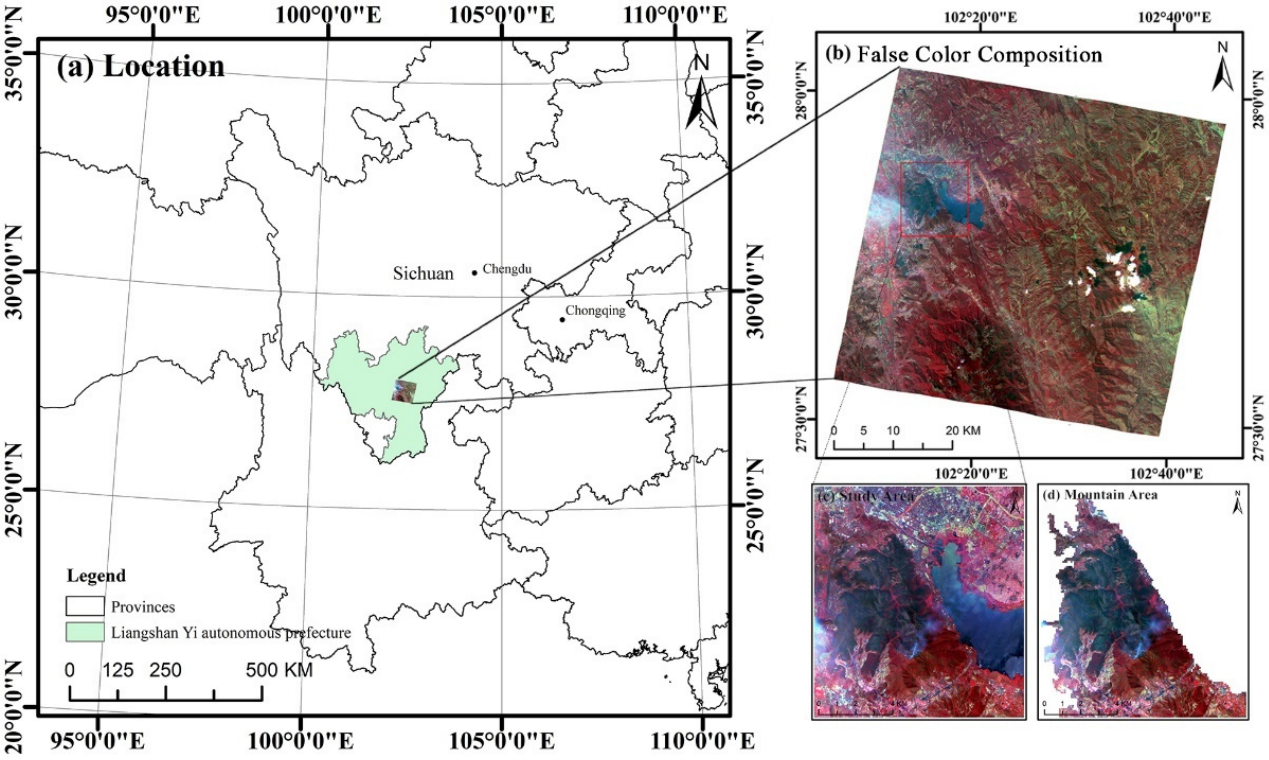

Figure 6. Schematic diagram showing the location of the study area: (**a**) Location of study area (a scene), (**b**) False-color composite map (post-fire), (**c**) False-color composite map of the study area (post-fire), (**d**) False-color composite map of the mountain area (post-fire).

At 15:51 on 30 March 2020, a hill fire broke out in Xichang City, Liangshan Prefecture, Sichuan Province, China. Due to high winds, the fire spread from the point of origin to the scenic area of the Lushan Mountains and quickly started burning the frontal body of the Lushan Mountains. Influenced by the changing wind direction, the fire produced multiple fire lines in different directions with low controllability and difficult rescue conditions. The combustion burn was not fully extinguished until 12:01 a.m. on 2 April 2020. This forest fire caused huge casualties and loss of forest area and is an important case for research into forest fire protection.

Zhuhai-1 satellite hyperspectral imagery (OHS) contains 32 spectral bands in the wavelength range 400–1000 nm, with a spectral resolution of 5–7 nm and a spatial resolution of 10 m. The joint observation network consisting of four satellites covers the globe once every two days, which allows it to quickly and accurately image fire-burned areas and provide fresh monitoring data for estimating fire areas [55]. This study uses two scenes of OHS hyperspectral images collected on 15 March 2020 (pre-fire) and 2 April 2020 (post-fire).

The Zhuhai-1 hyperspectral (OHS) data were preprocessed by using radiation calibration, atmospheric correction, and image clipping. Figure 7 shows the pre- and post-fire preprocessed false-color composite image of the study area.

Figure 7. Pre- and post-fire false-color composite map in the study area: (**a**) Study area on 15 March 2020 (pre-fire), (**b**) Study area on 2 April 2020 (post-fire).

3.2.2. Component Transformation

According to abundance variation characteristics of each component of the mixed image element described in the previous section, the original terrestrial objects (mainly vegetation cover and coverage in mountain fires) changed in areas, whether passed through by the fire or in the burned areas. Fire impacts on vegetation are not binary (burned/unburned) [12]; among them, the changes in the burned area are manifested mainly by the conversion of the original PV to NPV. Thus, the green photosynthetic characteristics of the original PV are destroyed by the fire, with leaf pigment reduction and desiccation (when leaves are scorched) [12], which are often manifested as dryness, shrinkage, etc. Based on the reduction in the leaf area index when leaves are burned [12], the change in the burned site is mainly manifested as the change of the original PV and NPV to BS, often manifested as scorching and blackening. The burned area includes the burned site. The BS component is not greatly affected by the fire [56], while the PV and NPV were altered to varying degrees pre- and post-fire. Based on this, the pre- and post-fire component transformation is derived (Figure 8).

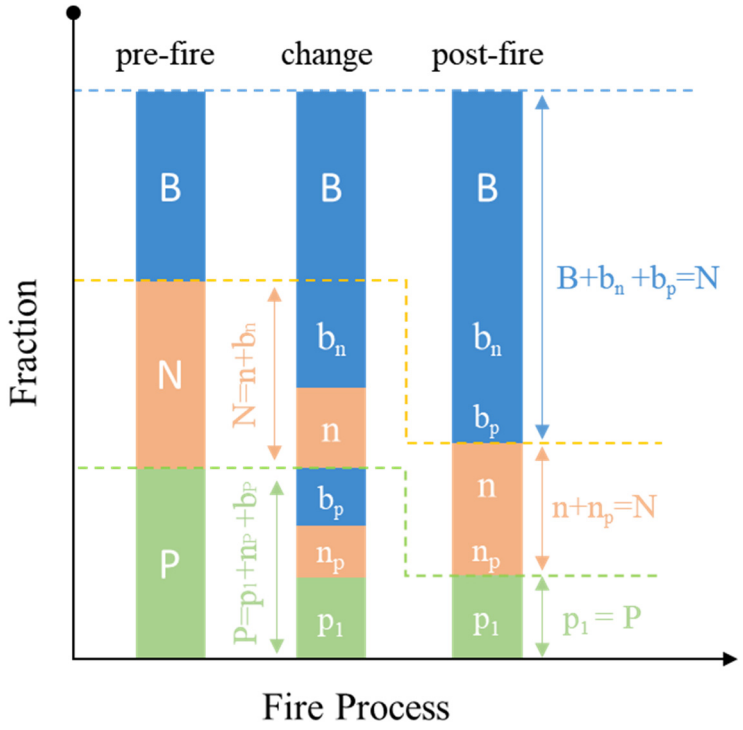

Figure 8. Pre-and post-fire component transformation.

Among them, B, N, and P are the BS, NPV, and PV that are in a more stable state and do not change pre- and post-fire, respectively; the corresponding lowercase letter represents that component after the change; the corner mark at the bottom right corner represents which other component the change component is transformed from. Combined with the pre-fire and post-fire component transformation, using geospatial analysis and other means, we can extract the changes of each category and count the area. The overfire area mainly includes b_p, n_p, and b_n, while the fire traces do not include n_p.

3.2.3. Changes in Cover of Each Fractions Pre- and Post-Forest Fire

The overall technical approach includes data preprocessing, calculation of coverage of each pixel fraction, and pre- and post-fire comparison of image characteristics, as well as an estimate of burned area. We compare pre- and post-fire images from both the study area and the mountain area, with detailed comparisons of the coverage and differences in each fraction.

The triangular persistence proves the triangular space method, which can be applied to extract the coverage of each component both pre-fire and post-fire. Before the three-fractional extraction of the study area, we removed the disturbing features to avoid the influence of post-fire image residual smoke and other effects. We used the NDWI [57] to extract pre-fire information about the water bodies in the study area. The digitally extracted vectors were used to remove the water bodies to avoid having the water bodies disturb the study. The water bodies were removed by masking the pre-fire and post-fire images according to the extent of the fire. After water removal, we also extracted the three pre-and post-fire land fractions (PV, NPV, BS) images. This strategy mainly involves index calculation, triangular space construction, and linear pixel unmixing. The final extraction results include three fractional coverages: NPV, PV, and BS. Triangular space construction here uses NSSI and NDVI, and their scatter plots and endmember selection appear in Figures 9 and 10, showing the pre- and post-fire extraction and composition.

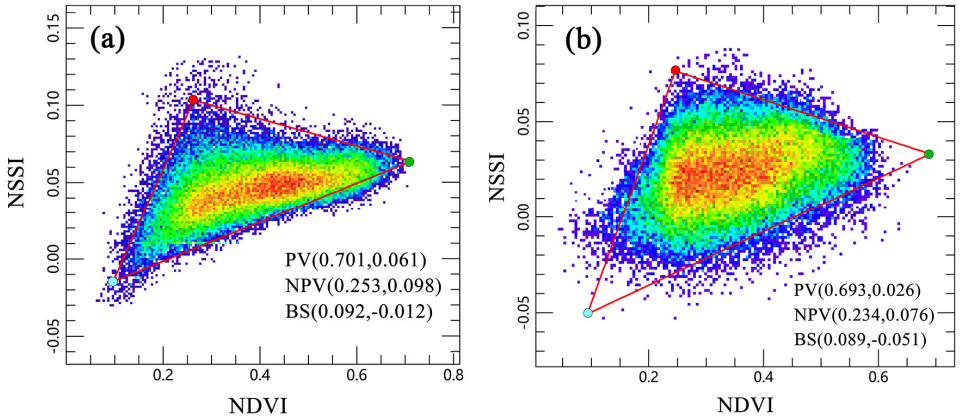

Figure 9. NSSI-NDVI scatter plot: (**a**) NSSI-NDVI scatterplot on 15 March 2020, (**b**) NSSI-NDVI scatterplot on 2 April 2020.

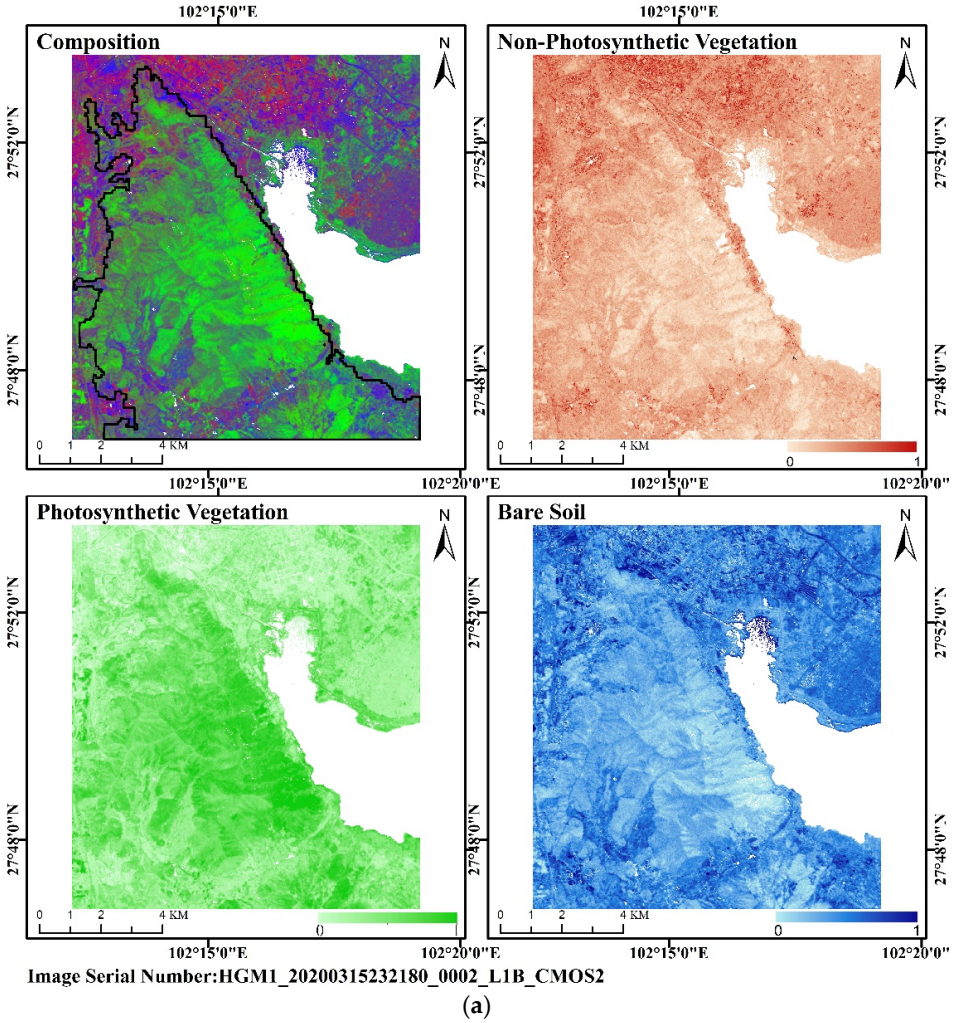

Figure 10. *Cont.*

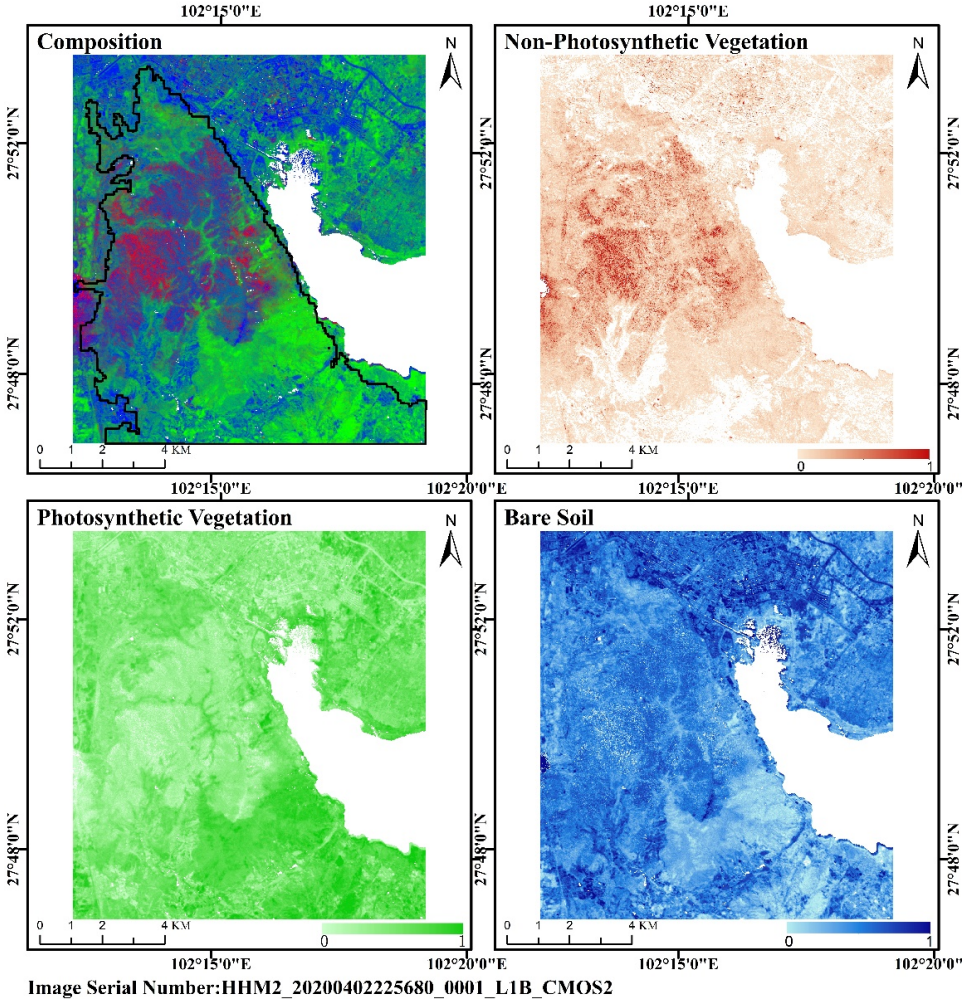

Figure 10. Three fractional results pre- and post- 3 0 March 2020 fire in Xichang: (**a**) Map of study area showing three land fractions on 15 March 2020 (pre-fire), (**b**) Map of study area showing three land fractions on 2 April 2020 (post-fire). (The map named composition is a composite of the other three fractions: r:NPV, g:PV, b:BS, the black vector range is the range of the extracted part of the mountain behind).

To better understand the fire-induced changes in distribution and coverage of each land fraction, the endmembers of each fraction are extracted according to the triangular space method and unmixed via linear hybrid pixel unmixing. The percentage of each fraction is then counted (Table 1). The results of the coverage comparison show that the NPV coverage in the study area significantly decreases, the PV coverage decreases, and the BS coverage increases after the fire.

Table 1. Comparison of pre-and post-fire coverage in the study area.

Comparison of Pre- and Post-Fire Fractional Coverage in Xichang City, Sichuan Province, 30 March 2020 (Study Area)				
		NPV	**PV**	**BS**
Fractional coverage	15 March 2020	36.0%	29.6%	34.4%
	2 April 2020	30.0%	26.6%	43.4%
	Difference	−6.0%	−3.0%	9.0%

Temporal limitations of OHS data meant that they were not available closer to the time of the fire. To determine whether differences in the data were caused by vegetation growth and other factors within 15 days of the fire, we compared Sentinel-2 MSI data from 15 March 2020 and from 30 March 2020. The results show that minimal changes in the morphology and endmember in the constructed NSSI-NDVI scatter results, and the normal phenological effects are negligible compared with the extent of disturbance of vegetation cover at the fire site. We thus used OHS 15-day data to characterize the vegetation cover of the study area pre-fire. It is not possible to quantitatively estimate how vegetation growth and other factors modify each fraction in the study area during the fire. Thus, we only extracted the burned area and burned site area from the fractional change, and do not discuss this in depth.

The comparison is further tuned to obtain the coverage situation after excluding terrestrial objects, which is more in line with the real situation, and the changes of each land fraction in the mountain area pre- and post-fire are determined (Table 2). The results of this land coverage comparison show that the pre- and post-fire changes in each land fraction in the mountain area are basically consistent with the changes in each land fraction in the study area. All results show a significant decrease in NPV coverage, a decrease in PV coverage, and an increase in BS coverage, which indicates that NPV and PV tends to convert to BS. However, comparing the two different ranges in the study area (i.e., study area versus mountain area), the fractional reduction in NPV coverage is greater in the mountain area where disturbing terrestrial objects are removed, whereas the fractional reduction in PV coverage decreases. Overall, more NPV converts to BS than does PV.

Table 2. Comparison of pre-and post-fire coverage in mountain area.

Comparison of Pre-and Post-Fire Fire Fractional Coverage in Xichang City, Sichuan Province, 30 March 2020 (Mountain Area)				
		NPV	**PV**	**BS**
Fractional coverage	15 March 2020	39.0%	24.0%	37.0%
	2 April 2020	29.6%	21.5%	48.9%
	Difference	−9.4%	−2.5%	11.9%

3.2.4. Estimation of Forest Fire Burned Area by Distinguishing NPV and PV

(1) Estimation of burned area

Using the pre-fire and post-fire component transformation (Section 3.2.1), the pre- and post-fire coverage of each component is used as an input source. To calculate the pre-fire and post-fire changes of each category using spatial analysis and other means, and the changes are updated and the area is counted.

First, the burned area is extracted. This includes the part converted by the fire from PV to NPV and from PV to BS and the part that converted from NPV to BS. The burn area includes the completely burned area, that is, the burned site but excludes the area converted from PV to NPV. The increase in BS is included. See Figure 11a for the portion of PV reduction ($n_p + b_p$). The portion of PV changed to BS is shown in Figure 11b: the area is 763 ha (b_p). In addition, the portion of PV changed to NPV (n_p) is shown in Figure 11c: the area of change is 594.6 ha. The decrease in NPV is 504.5 ha, as shown in Figure 11d. The total burn area is 1862.1 ha ($n_p + b_p + b_p$). The area of the burn site is 1267.5 ha ($b_p + b_p$).

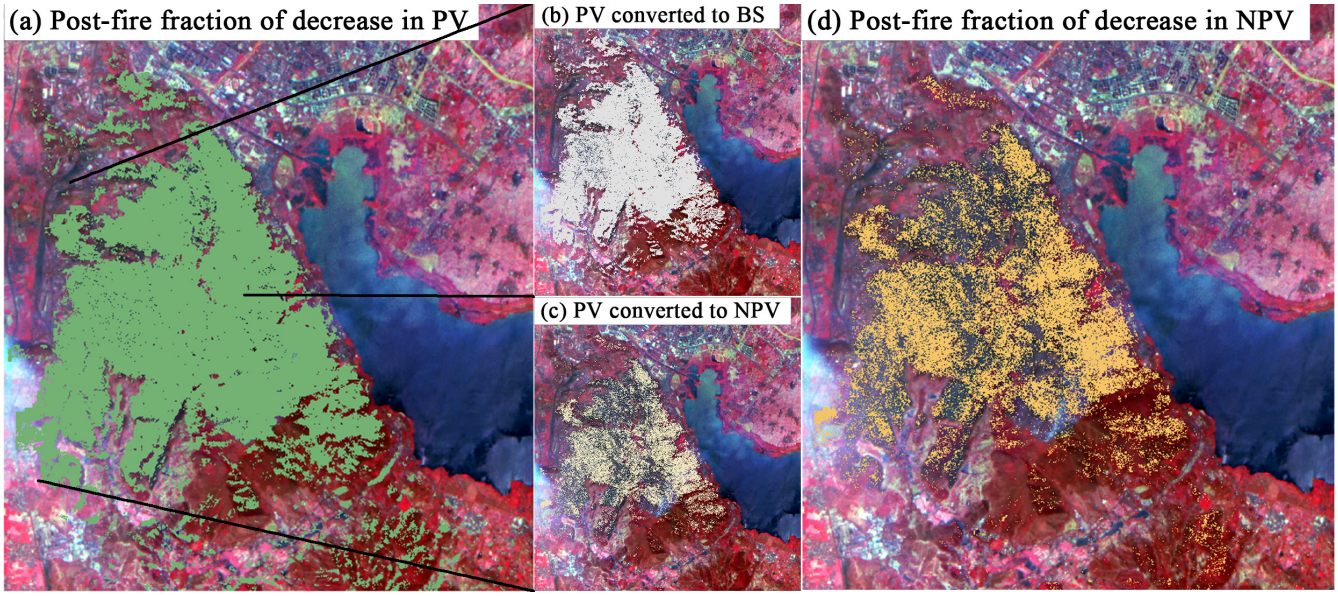

Figure 11. Post-fire extraction vector results for each land fraction (false-color composite image of study area): (**a**) Post-fire fraction of decrease in PV, (**b**) Post-fire fraction of PV converted to BS, (**c**) Post-fire fraction of PV converted to NPV, (**d**) Post-fire fraction of decrease in NPV.

(2) Accuracy validation

Since the existing burn area index (BAI) does well at extracting the area of a single category (i.e., the burn area) and fails to distinguish the area of burned area and the area of the burn site at the same time, the accuracy of the burned area obtained herein is verified by comparing it with the area extracted when using the BAI [58]. In this work, we use the bimodal histogram method [59] for threshold segmentation. The final threshold is 72.3 (Figure 12), and the segmentation is carried out with this value.

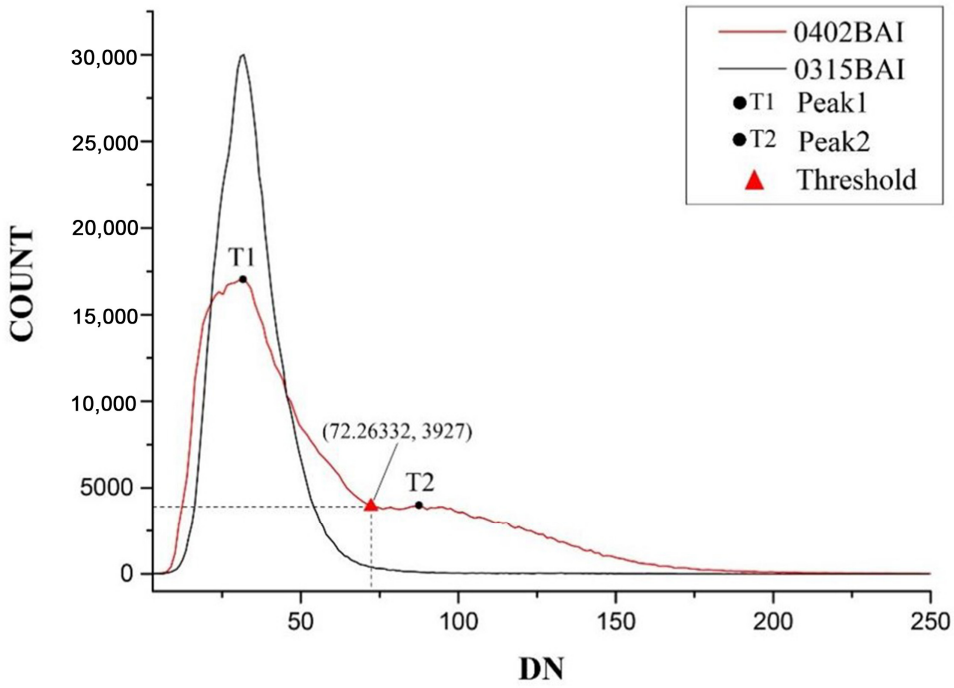

Figure 12. Bimodal histogram method to ensure threshold value of BAI.

Extracting the burn area by applying the BAI to the post-fire mountain area gives the results shown in Figure 13a, which show that the burn area is the bright area. After threshold selection, the extracted burn area appears as shown in Figure 13b, with an area of **1867.6** ha. Comparing the two extraction results shows that the error area is 5.5 ha, which is only **0.078%** of the total area. This result further demonstrates the accuracy of post-fire coverage extraction using the triangular space method.

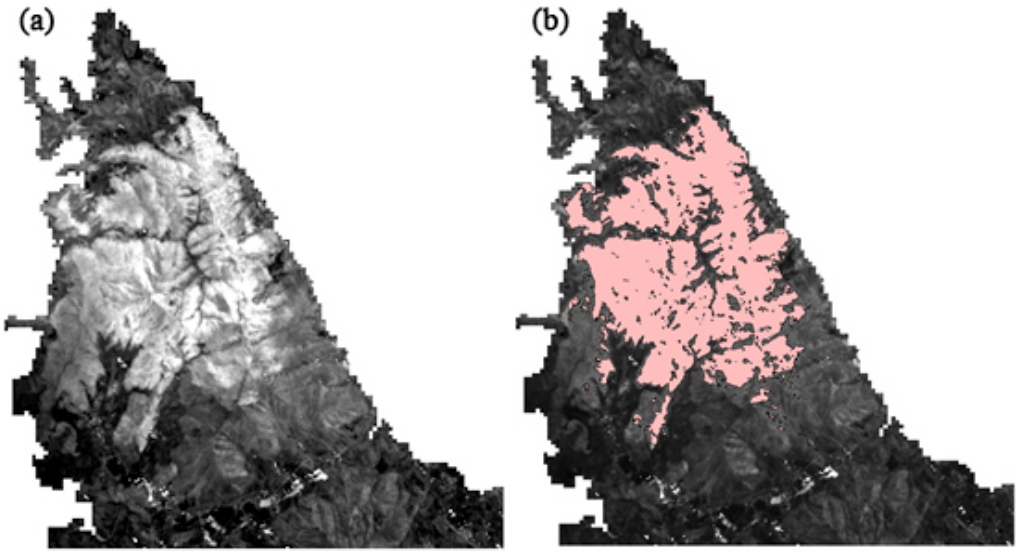

Figure 13. Extraction results of BAI and burn area (**a**) Mountain area BAI, (**b**) Extraction of burn area by applying BAI to mountain area.

4. Discussion and Conclusions

In both the fire simulation experiments and the fire ash wetting experiments, the triangular space exists. It demonstrates that the triangular space method can be used to estimate fractional coverage before and after fire. Based on the transformation characteristics of pre- and post-fire component coverage and the transformation model, the part that has changed through the firing process is extracted, and then the affected area is calculated. The results produce an estimated forest fire burned area of 1862.1 ha, and 1867.6 ha estimated from the BAI, leaving an error area of only 0.078% of the total area. These results demonstrate the accuracy of the proposed method.

This work estimates NPV, PV, and BS fractional cover of Zhuhai-1 satellite hyperspectral data (OHS) by applying the NSSI-NDVI triangular space method. The pre- and post-fire land categories are extracted from the data sensed on 30 March 2020 centered in Lushan, Sichuan Province. The comparison reveals that the pre-and post-fire difference in PV, NPV, and BS characterizes the forest fire loss and leads to accurate calculations of the burned area. The changes in NPV cover characterize a portion of the completely burned area, which accounts for 68% of the burned area. Thus, the extracted area of the burn site is 1267.5 ha, so the proposed method allows the burn site to be distinguished from the burn area.

The method can be applied to areas with different vegetation types and climates, and it meets a variety of satellite data requirements. The NSSI [47] index selected for the construction of the triangular space, which have the potential to be applied on Sentinel-2A/B and Sentinel-3 data, covering varied vegetation types. The index is designed to meet the needs of data used in the band 750–900 nm. The method has also been applied to the study of time-series data in southeastern China [60], and the study area involved in this paper has spanned nearly 20 degrees of latitude with good results.

The results of this study unveil new research directions. The fractional variations in the coverage of NPV, PV, and BS caused by forest fires, including dynamic fractional changes in direction and change ratio, reveal the changes caused by forest fires. These

results should be studied with temperature, wind speed, wind direction, and etc. So that the spread direction and speed of fire may be related to specific land covers and/or other factors. The integrity of fire burning can also be explored in relation to wind, topographic slope, pre-fire biomass load and structure, and water content. In addition, vegetation type significantly affects the detection of fire severity, and, due to the flammable nature of NPV, its coverage is associated with the risk and severity of fire. This can be combined with the distribution and coverage of NPV to establish wildfire warnings, and to map fire intensity and trends based on remote sensing images.

Author Contributions: X.W., J.Y. and Q.T. theorized this study and designed the experiment. X.W. and J.T. analyzed the data and drafted the manuscript. X.L. and J.Y. provided experimental data and suggestions for data processing. J.T. and C.Z. provided comments and suggestions for the manuscript and checked the writing. Q.T. and Q.L. provided comments and suggestions for the experiment. All authors have read and agreed to the published version of the manuscript.

Funding: This research was funded by the National Natural Science Foundation of China (grant number: 42101321) and the China Postdoctoral Science Foundation Project (grant number: 2021M701653).

Data Availability Statement: The data presented in this study are available on request from the corresponding author.

Acknowledgments: The authors acknowledge the Zhuhai Orbita Aerospace Science &Technology Co., Ltd. for data supply.

Conflicts of Interest: The authors declare no conflict of interest.

References

1. Kelly, L.T.; Brotons, L. Using fire to promote biodiversity. *Science* **2017**, *355*, 1264–1265. [CrossRef] [PubMed]
2. Chuvieco, E.; Aguado, I.; Yebra, M.; Nieto, H.; Salas, J.; Pilar Martin, M.; Vilar, L.; Martinez, J.; Martin, S.; Ibarra, P.; et al. Development of a framework for fire risk assessment using remote sensing and geographic information system technologies. *Ecol. Model.* **2010**, *221*, 46–58. [CrossRef]
3. Thonicke, K.; Spessa, A.; Prentice, I.C.; Harrison, S.P.; Dong, L.; Carmona-Moreno, C. The influence of vegetation, fire spread and fire behaviour on biomass burning and trace gas emissions: Results from a process-based model. *Biogeosciences* **2010**, *7*, 2191. [CrossRef]
4. Yue, C.; Ciais, P.; Cadule, P.; Thonicke, K.; van Leeuwen, T.T. Modelling the role of fires in the terrestrial carbon balance by incorporating SPITFIRE into the global vegetation model ORCHIDEE—Part 2: Carbon emissions and the role of fires in the global carbon balance. *Geosci. Model Dev.* **2015**, *8*, 1321–1338. [CrossRef]
5. Bowman, D.M.J.S.; Balch, J.K.; Artaxo, P.; Bond, W.J.; Carlson, J.M.; Cochrane, M.A.; D'Antonio, C.M.; DeFries, R.S.; Doyle, J.C.; Harrison, S.P.; et al. Fire in the Earth System. *Science* **2009**, *324*, 481–484. [CrossRef]
6. Lewis, S.L.; Edwards, D.P.; Galbraith, D. Increasing human dominance of tropical forests. *Science* **2015**, *349*, 827–832. [CrossRef]
7. Yuan, C.; Zhang, Y.; Liu, Z. A survey on technologies for automatic forest fire monitoring, detection, and fighting using unmanned aerial vehicles and remote sensing techniques. *Can. J. For. Res.* **2015**, *45*, 783–792. [CrossRef]
8. Dios, J.R.M.D.; Arrue, B.C.; Ollero, A.; Merino, L.; Gomez-Rodriguez, F. Computer vision techniques for forest fire perception. *Image Vision Comput.* **2008**, *26*, 550–562. [CrossRef]
9. Kolaric, D.; Skala, K.; Dubravic, A. Integrated system for forest fire early detection and management. *Period Biol.* **2008**, *110*, 205–211.
10. Daldegan, G.A.; Roberts, D.A.; Ribeiro, F.D.F. Spectral mixture analysis in Google Earth Engine to model and delineate fire scars over a large extent and a long time-series in a rainforest-savanna transition zone. *Remote Sens. Environ.* **2019**, *232*, 111340. [CrossRef]
11. Chuvieco, E. Global Impacts of Fire. In *Earth Observation of Wildland Fires in Mediterranean Ecosystems*; Chuvieco, E., Ed.; Springer: Berlin/Heidelberg, Germany, 2009; pp. 1–10.
12. Chuvieco, E.; Mouillot, F.; van der Werf, G.R.; San Miguel, J.; Tanase, M.; Koutsias, N.; Garcia, M.; Yebra, M.; Padilla, M.; Gitas, I.; et al. Historical background and current developments for mapping burned area from satellite Earth observation. *Remote Sens. Environ.* **2019**, *225*, 45–64. [CrossRef]
13. Arnett, J.T.T.R.; Coops, N.C.; Daniels, L.D.; Falls, R.W. Detecting forest damage after a low-severity fire using remote sensing at multiple scales. *Int. J. Appl. Earth Obs.* **2015**, *35*, 239–246. [CrossRef]
14. Chu, T.; Guo, X.L.; Takeda, K. Temporal dependence of burn severity assessment in Siberian larch (*Larix sibirica*) forest of northern Mongolia using remotely sensed data. *Int. J. Wildland Fire* **2016**, *25*, 685–698. [CrossRef]
15. Fernandez-Manso, A.; Quintano, C. Evaluating Landsat ETM+ emissivity-enhanced spectral indices for burn severity discrimination in Mediterranean forest ecosystems. *Remote Sens. Lett.* **2015**, *6*, 302–310. [CrossRef]

16. Chuvieco, E.; Riano, D.; Danson, F.M.; Martin, P. Use of a radiative transfer model to simulate the postfire spectral response to burn severity. *J. Geophys. Res.-Biogeol.* **2006**, *111*, G000143. [CrossRef]
17. De Santis, A.; Chuvieco, E. Burn severity estimation from remotely sensed data: Performance of simulation versus empirical models. *Remote Sens. Environ.* **2007**, *108*, 422–435. [CrossRef]
18. De Santis, A.; Chuvieco, E. GeoCBI: A modified version of the Composite Burn Index for the initial assessment of the short-term burn severity from remotely sensed data. *Remote Sens. Environ.* **2009**, *113*, 554–562. [CrossRef]
19. Chiang, S.H.; Ulloa, N.I. Mapping and Tracking Forest Burnt Areas in the Indio Maiz Biological Reserve Using Sentinel-3 SLSTR and VIIRS-DNB Imagery. *Sensors* **2019**, *19*, 5423. [CrossRef]
20. Dos Santos, S.M.B.; Bento-Goncalves, A.; Franca-Rocha, W.; Baptista, G. Assessment of Burned Forest Area Severity and Postfire Regrowth in Chapada Diamantina National Park (Bahia, Brazil) Using dNBR and RdNBR Spectral Indices. *Geosciences* **2020**, *10*, 106. [CrossRef]
21. Lentile, L.B.; Smith, A.M.S.; Hudak, A.T.; Morgan, P.; Bobbitt, M.J.; Lewis, S.A.; Robichaud, P.R. Remote sensing for prediction of 1-year post-fire ecosystem condition. *Int. J. Wildland Fire* **2009**, *18*, 594–608. [CrossRef]
22. Lentile, L.B.; Holden, Z.A.; Smith, A.M.S.; Falkowski, M.J.; Hudak, A.T.; Morgan, P.; Lewis, S.A.; Gessler, P.E.; Benson, N.C. Remote sensing techniques to assess active fire characteristics and post-fire effects. *Int. J. Wildland Fire* **2006**, *15*, 319–345. [CrossRef]
23. Hawbaker, T.J.; Vanderhoof, M.K.; Beal, Y.J.; Takacs, J.D.; Schmidt, G.L.; Falgout, J.T.; Williams, B.; Fairaux, N.M.; Caldwell, M.K.; Picotte, J.J.; et al. Mapping burned areas using dense time-series of Landsat data. *Remote Sens. Environ.* **2017**, *198*, 504–522. [CrossRef]
24. Mouillot, F.; Schultz, M.G.; Yue, C.; Cadule, P.; Tansey, K.; Ciais, P.; Chuvieco, E. Ten years of global burned area products from spaceborne remote sensing-A review: Analysis of user needs and recommendations for future developments. *Int. J. Appl. Earth Obs.* **2014**, *26*, 64–79. [CrossRef]
25. Jia, G.J.; Burke, I.C.; Goetz, A.F.H.; Kaufmann, M.R.; Kindel, B.C. Assessing spatial patterns of forest fuel using AVIRIS data. *Remote Sens. Environ.* **2006**, *102*, 318–327. [CrossRef]
26. Wang, S. *Fuel Spatial Distribution and Potential Fire Behavior of Major Coniferous Forests in Southwest Sichuan, China*; Beijing Forestry University: Beijing, China, 2016.
27. Elmore, A.J.; Asner, G.P.; Hughes, R.F. Satellite monitoring of vegetation phenology and fire fuel conditions in Hawaiian drylands. *Earth Interact.* **2005**, *9*, 1–21. [CrossRef]
28. Wang, G.; Wang, J.; Zou, X.; Han, L.; Zong, M. A Review on Estimating Fractional Cover of Non-photosynthetic Vegetation by Using Remote Sensing. *Remote Sens. Technol. Appl.* **2018**, *33*, 1–9.
29. Jia, K.; Li, Y.W.; Liang, S.L.; Wei, X.Q.; Yao, Y.J. Combining Estimation of Green Vegetation Fraction in an Arid Region from Landsat 7 ETM+ Data. *Remote Sens.* **2017**, *9*, 1121. [CrossRef]
30. Yang, J.; Weisberg, P.J.; Bristow, N.A. Landsat remote sensing approaches for monitoring long-term tree cover dynamics in semi-arid woodlands: Comparison of vegetation indices and spectral mixture analysis. *Remote Sens. Environ.* **2012**, *119*, 62–71. [CrossRef]
31. Cochrane, M.A.; Souza, C.M. Linear mixture model classification of burned forests in the Eastern Amazon. *Int. J. Remote Sens.* **1998**, *19*, 3433–3440. [CrossRef]
32. Li, X.D.; Zhang, H.Y.; Yang, G.B.; Ding, Y.L.; Zhao, J.J. Post-Fire Vegetation Succession and Surface Energy Fluxes Derived from Remote Sensing. *Remote Sens.* **2018**, *10*, 1000. [CrossRef]
33. Roberts, S.D.; Harrington, C.A.; Terry, T.A. Harvest residue and competing vegetation affect soil moisture, soil temperature, N availability, and Douglas-fir seedling growth. *For. Ecol. Manag.* **2005**, *205*, 333–350. [CrossRef]
34. Schillinger, W.F.; Young, D.L.; Kennedy, A.C.; Paulitz, T.C. Diverse no-till irrigated crop rotations instead of burning and plowing continuous wheat. *Field Crops Res.* **2010**, *115*, 39–49. [CrossRef]
35. Varga, T.A.; Asner, G.P. Hyperspectral and lidar remote sensing of fire fuels in Hawaii Volcanoes National Park. *Ecol. Appl.* **2008**, *18*, 613–623. [CrossRef]
36. Xuan, H. *Research on Fire Monitoring with High Time and High Spatial Resolution Based on Multi-Source Remote Sensing Data*; University of Electronic Science and Technology of China: Chengdu, China, 2020.
37. Morton, D.C.; DeFries, R.S.; Nagol, J.; Souza, C.M.; Kasischke, E.S.; Hurtt, G.C.; Dubayah, R. Mapping canopy damage from understory fires in Amazon forests using annual time series of Landsat and MODIS data. *Remote Sens. Environ.* **2011**, *115*, 1706–1720. [CrossRef]
38. Qin, X.L.; Li, Z.Y.; Yi, H.R.; Chen, E.X.; Pang, Y. Studying On Burned Scar Mapping Using ENVISAT-MERIS Data. *Remote Sens. Technol. Appl.* **2008**, *1*, 1–6.
39. Chuvieco, E.; Lizundia-Loiola, J.; Pettinari, M.L.; Ramo, R.; Padilla, M.; Tansey, K.; Mouillot, F.; Laurent, P.; Storm, T.; Heil, A.; et al. Generation and analysis of a new global burned area product based on MODIS 250 m reflectance bands and thermal anomalies. *Earth Syst. Sci. Data* **2018**, *10*, 2015–2031. [CrossRef]
40. Noojipady, P.; Morton, D.C.; Macedo, M.N.; Victoria, D.C.; Huang, C.Q.; Gibbs, H.K.; Bolfe, E.L. Forest carbon emissions from cropland expansion in the Brazilian Cerrado biome. *Environ. Res. Lett.* **2017**, *12*, 025004. [CrossRef]
41. Urbanski, S.P.; Reeves, M.C.; Corley, R.E.; Silverstein, R.P.; Hao, W.M. Contiguous United States wildland fire emission estimates during 2003–2015. *Earth Syst. Sci. Data* **2018**, *10*, 2241–2274. [CrossRef]

42. Li, S. *Extraction of Forest Burned Area Based on Stacked ConvLSTM and Remote Sensing Image Time Series*; University of Chinese Academy of Science: Beijing, China, 2021.
43. Andela, N.; Morton, D.C.; Giglio, L.; Chen, Y.; van der Werf, G.R.; Kasibhatla, P.S.; DeFries, R.S.; Collatz, G.J.; Hantson, S.; Kloster, S.; et al. A human-driven decline in global burned area. *Science* **2017**, *356*, 1356–1361. [CrossRef]
44. Guerschman, J.P.; Hill, M.J.; Renzullo, L.J.; Barrett, D.J.; Marks, A.S.; Botha, E.J. Estimating fractional cover of photosynthetic vegetation, non-photosynthetic vegetation and bare soil in the Australian tropical savanna region upscaling the EO-1 Hyperion and MODIS sensors. *Remote Sens. Environ.* **2009**, *113*, 928–945. [CrossRef]
45. Vila, J.P.S.; Barbosa, P. Post-fire vegetation regrowth detection in the Deiva Marina region (Liguria-Italy) using Landsat TM and ETM plus data. *Ecol. Model.* **2010**, *221*, 75–84. [CrossRef]
46. Gibson, R.; Danaher, T.; Hehir, W.; Collins, L. A remote sensing approach to mapping fire severity in south-eastern Australia using sentinel 2 and random forest. *Remote Sens. Environ.* **2020**, *240*, 111702. [CrossRef]
47. Tian, J.; Su, S.S.; Tian, Q.J.; Zhan, W.F.; Xi, Y.B.; Wang, N. A novel spectral index for estimating fractional cover of non-photosynthetic vegetation using near-infrared bands of Sentinel satellite. *Int. J. Appl. Earth Obs.* **2021**, *101*, 102361. [CrossRef]
48. Yue, J.B.; Tian, Q.J. Estimating fractional cover of crop, crop residue, and soil in cropland using broadband remote sensing data and machine learning. *Int. J. Appl. Earth Obs.* **2020**, *89*, 102089. [CrossRef]
49. Shu, L.; Wang, M.; Tian, X.; Zhang, X.; Dai, X.a. Calculation and Description of Forest Fire Behavior Characters. *Sci. Silvae Sin.* **2004**, *40*, 179–183.
50. Liu, Z.-H.; Chang, Y.; He, H.-S.; Hu, Y.-M.; Wang, W.-J. Effects of different forest fuel treatments on potential forest fire regimes in Great Xing'an Mountains: A simulation study. *Shengtaixue Zazhi* **2009**, *28*, 1462–1469.
51. Qin, X.L.; Zhang, Z.H.; Yi, H.R.; Ji, P. A Methodology to Predict the Moisture of Forest Fuels. *Fire Saf. Sci.* **2001**, *10*, 159.
52. Xiao, S. *Research on Modelling of Surface Dead Fuel Moisture Content of Main Forest Types in Xishan Mountain of Beijing*; Beijing Forestry University: Beijing, China, 2015.
53. Lifang, M. *Research on Moisture Prediction of Forest-Floor Fuel*; Beijing Forestry University: Beijing, China, 2011.
54. Hong, L.; LI, W.C.; OuYang, Y.; Zhang, J.H.; Zhang, T.J.; Li, Y.G.; Huang, H.X.; Huang, Y.; Li, F.; Chen, M.; et al. Exploration and ractice of the compilation of ecological geology series maps based on geological formations research, mountainous region in Southwest China—Exemplified by Qionghai-Lushan area, western margin of Yangtze Block. *Acta Geol. Sin.* **2022**, 1–16.
55. Hang, J.; Qian, Y.Y.; Zheng, S.A.; He, H.Q. Analysis of advantages of Gaofen satellite and other commercial remote sensing data applications in key industries. *Dual Use Technol. Prod.* **2022**, 4–9.
56. Quintano, C.; Fernandez-Manso, A.; Fernandez-Manso, O.; Shimabukuro, Y.E. Mapping burned areas in Mediterranean countries using spectral mixture analysis from a uni-temporal perspective. *Int. J. Remote Sens.* **2006**, *27*, 645–662. [CrossRef]
57. Gao, B.C. NDWI—A normalized difference water index for remote sensing of vegetation liquid water from space. *Remote Sens. Environ.* **1996**, *58*, 257–266. [CrossRef]
58. Chuvieco, E.; Martín, M.P. *Cartografía de Grandes Incendios Forestales en la Península Ibérica a Partir de Imágenes NOAA-AVHRR*; CSIC: Madri, Spain, 1998.
59. Prewitt, J.M.S.; Mendelsohn, M.L. Analysis of cell images. *Ann. N. Y. Acad. Sci.* **1966**, *128*, 1035. [CrossRef] [PubMed]
60. Zhu, C.; Tian, J.; Tian, Q.; Wang, X.; Li, Q. Using NDVI-NSSI feature space for simultaneous estimation of fractional cover of non-photosynthetic vegetation and photosynthetic vegetation. *Int. J. Appl. Earth Obs.* **2023**, *118*, 103282. [CrossRef]